



Repositorio Institucional de la Universidad Autónoma de Madrid

<https://repositorio.uam.es>

Esta es la **versión de autor** del artículo publicado en:

This is an **author produced version** of a paper published in:

Nanoscale 8.23 (2016): 11818-11826

DOI: <http://dx.doi.org/10.1039/c5nr07445b>

Copyright: © 2016 The Royal Society of Chemistry

El acceso a la versión del editor puede requerir la suscripción del recurso

Access to the published version may require subscription

High resolution Atomic Force Microscopy of double-stranded RNA[†]

*Pablo Ares,^a Maria Eugenia Fuentes-Perez,^b Elías Herrero-Galán,^b José M. Valpuesta,^b Adriana Gil,^b Julio Gomez-Herrero,^{*a,c} and Fernando Moreno-Herrero^{*b}*

^a Department of Condensed Matter Physics. Universidad Autónoma de Madrid. E-28049 Madrid, Spain. E-mail: julio.gomez@uam.es.

^b Department of Macromolecular Structures, Centro Nacional de Biotecnología, Consejo Superior de Investigaciones Científicas, 28049 Cantoblanco, Madrid, Spain. E-mail: fernando.moreno@cnb.csic.es.

^c Condensed Matter Physics Center (IFIMAC), Universidad Autónoma de Madrid, E-28049, Madrid, Spain.

[†] Electronic Supplementary Information (ESI) available.

*Corresponding Authors

KEYWORDS: double-stranded RNA (dsRNA), atomic force microscopy (AFM), double helix, high resolution.

ABSTRACT:

Double-stranded (ds) RNA mediates suppression of specific gene expression, it is the genetic material of a number of viruses, and a key activator of the innate immune response against viral infections. The ever increasing list of roles played by dsRNA in the cell and its potential biotechnological applications has raised over the last decade an interest for the characterization of its mechanical properties and structure, and that includes approaches using Atomic Force Microscopy (AFM) and other single-molecule techniques. Recent reports have resolved the structure of dsDNA with AFM at unprecedented resolution. However, an equivalent study with dsRNA is still lacking. Here, we have visualized the double helix of dsRNA under near-physiological conditions and at enough resolution to resolve the A-form sub-helical pitch periodicity. We have employed different high-sensitive force-detection methods and obtained images with similar spatial resolution. Therefore, we show here that the limiting factors for high-resolution AFM imaging of soft material in liquid medium are, rather than the imaging mode, the force between tip and sample and the sharpness of the tip apex.

INTRODUCTION

For many years, RNA was considered only as the molecule involved in the readout of information stored in DNA. Today, we know that RNA plays critical roles not only in transmission but also in gene regulation, and that it can even be catalytic, carrying out biochemical reactions like proteins do. The discovery of gene silencing by RNA in its double-stranded form (dsRNA) added an additional dimension to a molecule that was primarily considered to be single-stranded. Moreover, the fact that a variety of viruses store their genetic material in dsRNA, and that this molecule appears as an activator for the immune response against viral attacks, revealed dsRNA as an interesting molecule with potential biotechnological applications. It is thus not surprising the recent interest for the characterization of its mechanical properties using mainly single-molecule techniques that include atomic force microscopy, magnetic tweezers, and optical tweezers.¹⁻³

While extensive work has been already performed with dsDNA, a high-resolution Atomic Force Microscopy imaging study of dsRNA has not been carried out so far. This is very likely because of the higher complexity of imaging the dsRNA structure, where the major and minor grooves have similar dimensions and because methods to equilibrate dsRNA molecules on flat surfaces have only been recently reported.² The helical regularity of DNA was first observed in contact mode AFM in a seminal work by Mou et al.⁴ However, contact imaging proved not to be the best option for imaging biological materials, and other dynamic modes that minimize shear forces are usually preferred with respect to classic contact mode.⁵ Among them, Amplitude Modulation AM-AFM (also known as Tapping or intermittent contact) is the most used for both air,^{6,7} and liquid environments,^{8,9} and has been proven to achieve high resolution on different biological samples,¹⁰⁻¹³ including the double helix of DNA.¹⁴⁻¹⁷ Other dynamic modes such as Frequency Modulation (FM-AFM),¹⁸⁻²¹ or Drive Amplitude Modulation (DAM-AFM),²² are also used to obtain high resolution in liquid medium. This degree of resolution is possible because oscillation amplitudes are adjusted to a value in the same order as the decay length of the interaction force between tip and sample.²³ Indeed, the minor and major grooves of dsDNA have been resolved in FM-AFM.²⁴ Other intermittent contact imaging modes such as PeakForce Tapping²⁵ or Jumping Mode plus (JM+),²⁶ allow to detect tip-sample interactions at angstrom precision with piconewton sensitivity. As an example, Pyne and coworkers reported high resolution images of dsDNA using PeakForce AFM.¹⁷

Each imaging technique accurately controls on different parameters, either the cantilever oscillation amplitude and phase or the force. In dynamic modes (AM-AFM, FM-AFM), the relevant parameters are the cantilever oscillation amplitude and the phase between the cantilever excitation signal and its oscillatory response. In force-distance based imaging modes such as PeakForce or JM+, the relevant parameter is the force, which is directly controlled to probe the sample. We will argue below that provided a sharp tip and the best possible working conditions for each AFM imaging mode, high-resolution on soft biological samples can be achieved in liquid environment nearly independently of the imaging mode.^{5,27}

In this work, we have first used dsDNA as a molecular standard for high-resolution to adjust the experimental and operational conditions to image nucleic acids in liquid, reproducing recently published

results.^{16, 17, 24} We have then imaged for the first time dsRNA with a lateral resolution enough to resolve a ~ 1.5 nm periodicity (half a full helical turn) compatible with the A-form of dsRNA. High resolution images of dsRNA have been obtained using AM-AFM, DAM-AFM, and JM+ using oscillation amplitudes in dynamic modes lower than ~ 1 nm, and applied forces in intermittent contact imaging modes in the order of tens of pN. Finally, simulations of AFM images of dsRNA with different tip radius and comparison with experimental images have revealed that high-resolution imaging for these structures requires sharp tips with a radius smaller than ~ 2.5 nm.

RESULTS AND DISCUSSION

We first set up experimental conditions compatible with different imaging modes for high-resolution AFM imaging of dsDNA so these could be later applied to dsRNA. Standard methods to adsorb dsDNA on mica use Mg^{2+} as divalent cation but this methodology failed to equilibrate dsRNA on mica.¹ Therefore, we employed Ni^{2+} as a divalent cation to equilibrate both dsDNA and dsRNA molecules on mica following published protocols (see ² and the Experimental section for details on sample preparation). In order to compare the high-resolution capability of dynamic and force-distance imaging modes we chose a cantilever suitable for both kinds of working modes. We used biolever-mini type cantilevers from Olympus (BL-AC40TS-C2) with specifications of tip radius ~ 8 nm, resonance frequency in liquid ~ 25 kHz, and low spring constant ~ 0.09 N $\cdot\text{m}^{-1}$ (see Experimental section for details). Their relatively high resonance frequency in liquids makes them appropriate for use in dynamic modes. Similarly their low spring constant is required to minimize the applied load in force-distance based imaging modes.

We imaged dsDNA molecules adsorbed on a mica surface in liquid environment using AM-AFM with cantilever oscillation amplitude of 0.7 nm (**Fig. 1a**). Scan rates and feedback parameters were adjusted for optimum contrast and stability. Despite an obvious effect of tip-sample dilation that makes dsDNA strands look wider than the expected 2-nm crystallographic width, a periodic corrugation can be observed within the molecules. **Fig. 1b** shows this corrugation in detail. We found a very good agreement between the B-form model for dsDNA structure (**Fig. 1c**) with the profile dimensions (**Fig. 1d**), which periodicity can be attributed to the major and minor grooves of the dsDNA helical structure with a helical pitch of 3.4 ± 0.3 nm. The resolution achieved is comparable to that reported in previous AFM studies,^{15-17, 24, 28} proving that our setup has the required stability and resolution to attempt to image nucleic acids at the nanometer scale.

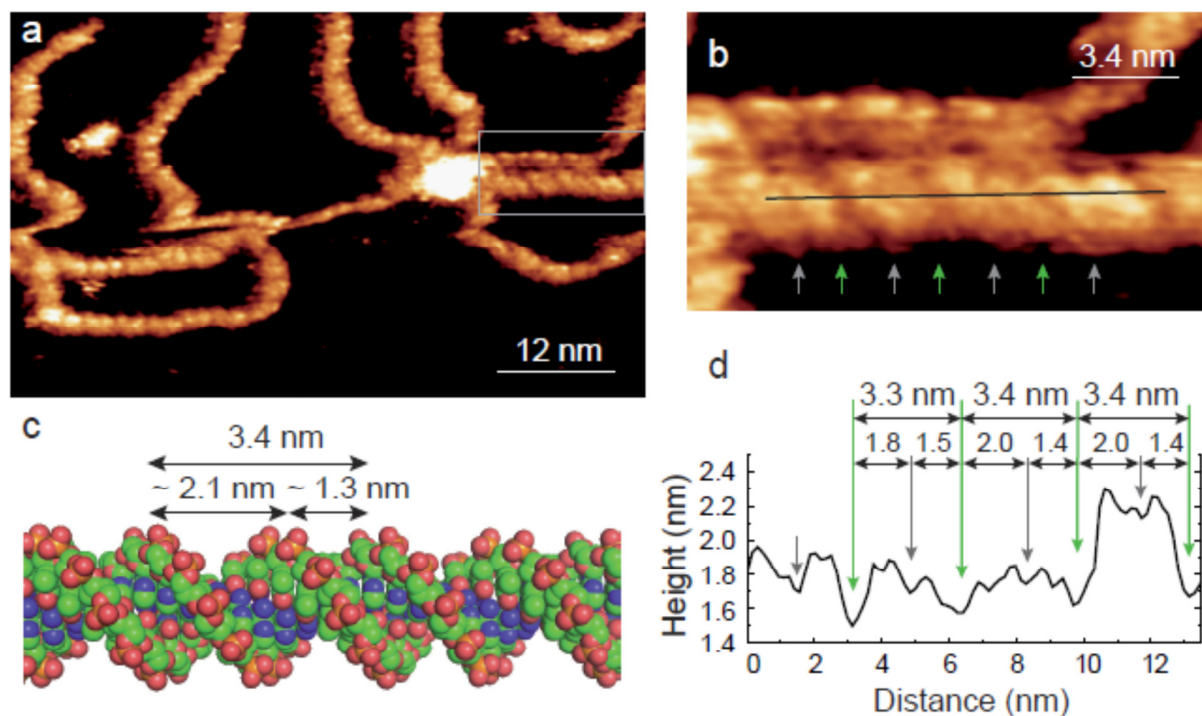


Fig. 1. High-resolution imaging of dsDNA using AM-AFM. (a) A periodic corrugation and a helical structure along the molecule are observed. (b) Detail at higher magnification of (a) that highlights the double-band corrugation corresponding to the major (green arrow) and minor (gray arrow) grooves. (c) Model of dsDNA showing relevant dimensions. (d) Height profile along the line in (b). Color scale (from dark to bright) in (a) and (b) was adjusted to enhance the corrugation observed along the dsDNA (2.9 nm total range in (a) and 1.7 nm in (b)).

Next, we decided to apply similar procedures to image dsRNA molecules adsorbed on mica following published protocols that use NiCl_2 .² The sample was prepared as described in the Experimental section and imaged in liquid using AM-AFM with identical imaging conditions as previously described for dsDNA (Fig. 2a, see Table 1 and S1 for a summary of imaging conditions). In the example shown (Fig. 2b), a profile taken along the axis of the molecule allowed us to measure a distance between valleys of 1.5-1.7 nm that could be attributed within error to the corresponding dimensions of both the major and minor grooves of the A-form structure of dsRNA (Fig. 2c and Fig. 2d). However, in most of the cases, we could only identify a single periodicity of 3.2 ± 0.3 nm that coincides with the helical pitch of dsRNA.

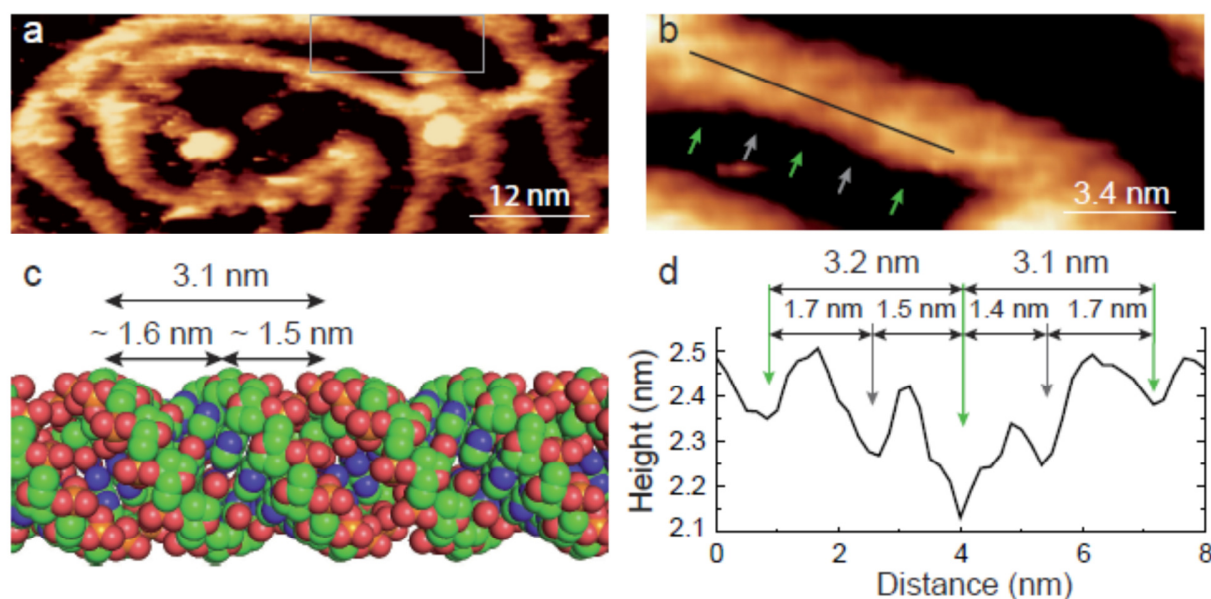


Fig. 2. High-resolution imaging of dsRNA using AM-AFM. (a) A narrower periodic corrugation compared to dsDNA was observed in dsRNA molecules. (b) Detail at higher magnification of (a). Occasionally, we observed a monotonic periodicity compatible with the presence of the major and minor grooves (marked in the figure with green and grey arrows), but this was not always achievable. (c) Model of dsRNA showing relevant dimensions. (d) Height profile along the line in b. Color scale (from dark to bright) in (a) and (b) was adjusted to enhance the corrugation observed along the dsRNA (1.4 nm total range in (a) and 1.2 nm total range in (b)).

Table 1. Experimental conditions of different imaging modes employed in this study.

Imaging Mode	Image Size (nm)	Scan Rate (lines s ⁻¹)	Imaging Amplitude (nm)	Dissipation (fW)	Force (pN)
AM-AFM (dsDNA)	80	3.7	0.7		
AM-AFM (dsRNA)	80	4.3	0.6		
DAM-AFM (dsRNA)	75	6.5	0.6	0.3	
JM+ (dsRNA)	75	3	15-35*		35

* Tip excursion

Counter-intuitively, the minor groove of dsRNA (~1.5 nm) was in general more difficult to observe than the minor groove of dsDNA (~1.3 nm), even though the former is wider and identical working conditions were employed for imaging both samples (compare **Fig. 1d** and **Fig. 2d**). A possible explanation could be the particular orientation and distance of the phosphate groups (red spheres in models) of each strand of dsRNA. Phosphate groups in dsRNA are facing each other and leave a narrower minor groove than in dsDNA, where phosphate groups appear in the outer edges of the double helix pointing outwards. This particular orientation of phosphate groups in dsRNA has been suggested as a possible reason for the inability to adsorb dsRNA on mica using Mg^{2+} ,¹ and may also be the reason why the AFM tip cannot resolve the minor groove in RNA samples precluding its frequent visualization. Alternatively, if the mechanism for dsRNA adsorption to the mica surface involves base complexation with Ni^{2+} and dislocation,² it may affect the overall secondary structure of dsRNA, hampering the visualization of the minor groove.

In order to get further insight into the mechanisms for the high resolution imaging of soft biological samples in liquids, we decided to image dsRNA molecules using other AFM imaging modes (**Fig. 3**). AM-AFM, DAM-AFM and JM+ were used under conditions of low invasiveness with small oscillating amplitudes, low dissipation power, and small contact force, respectively (**Table 1** and **S1**). In all cases, high resolution was obtained allowing the observation of at least a single periodicity along the dsRNA molecules (**Fig. 3a-c**). The level of invasiveness and damage of the different imaging modes was assessed by the measurement of dsRNA height and its comparison with consecutive images. This is sensible because AFM heights critically depend on the force that the AFM tip applies to the nucleic acid.^{17, 24, 29} The height of several dsRNA molecules obtained with the three imaging modes employed was nearly identical and of about 2.5 ± 0.3 nm in agreement with the crystallographic dimensions of 2.6 nm for the dsRNA (**Fig. 3d**). The helical pitch was also clearly resolved independently of the measuring mode (**Fig. 3e**). We measured the helical pitch along different segments over the same molecule and also on different molecules. Overall we measured along 8, 13, and 14 molecules that resulted in 64, 116 and 114 data values for AM-AFM, DAM-AFM, and JM+, respectively. Each distribution was fitted with a Gaussian function with similar mean values and standard deviations, independently of the imaging mode. The mean periodicity was 3.1 ± 0.3 nm (*mean \pm standard deviation (SD)*), a value consistent with the A-form structure of dsRNA. Indeed, a rise per base pair of 0.29 nm has been directly measured with AFM for dsRNA,² and that gives a distance of 3.19 nm for the 11 bases contained in a single turn of the A-form structure of dsRNA. The wide distributions described here (**Fig. 3e**) are consistent with the structural irregularities previously reported.^{17, 24} We believe this variability may be induced by the strong electrostatic interaction with the mica caused by Ni^{2+} cations. Together, these data show that a similar high resolution can be obtained regardless of the imaging mode employed when working at optimal operating conditions. Similar conclusions when working with different feedback architectures and/or applied to other biological samples have been reported elsewhere.^{5, 27}

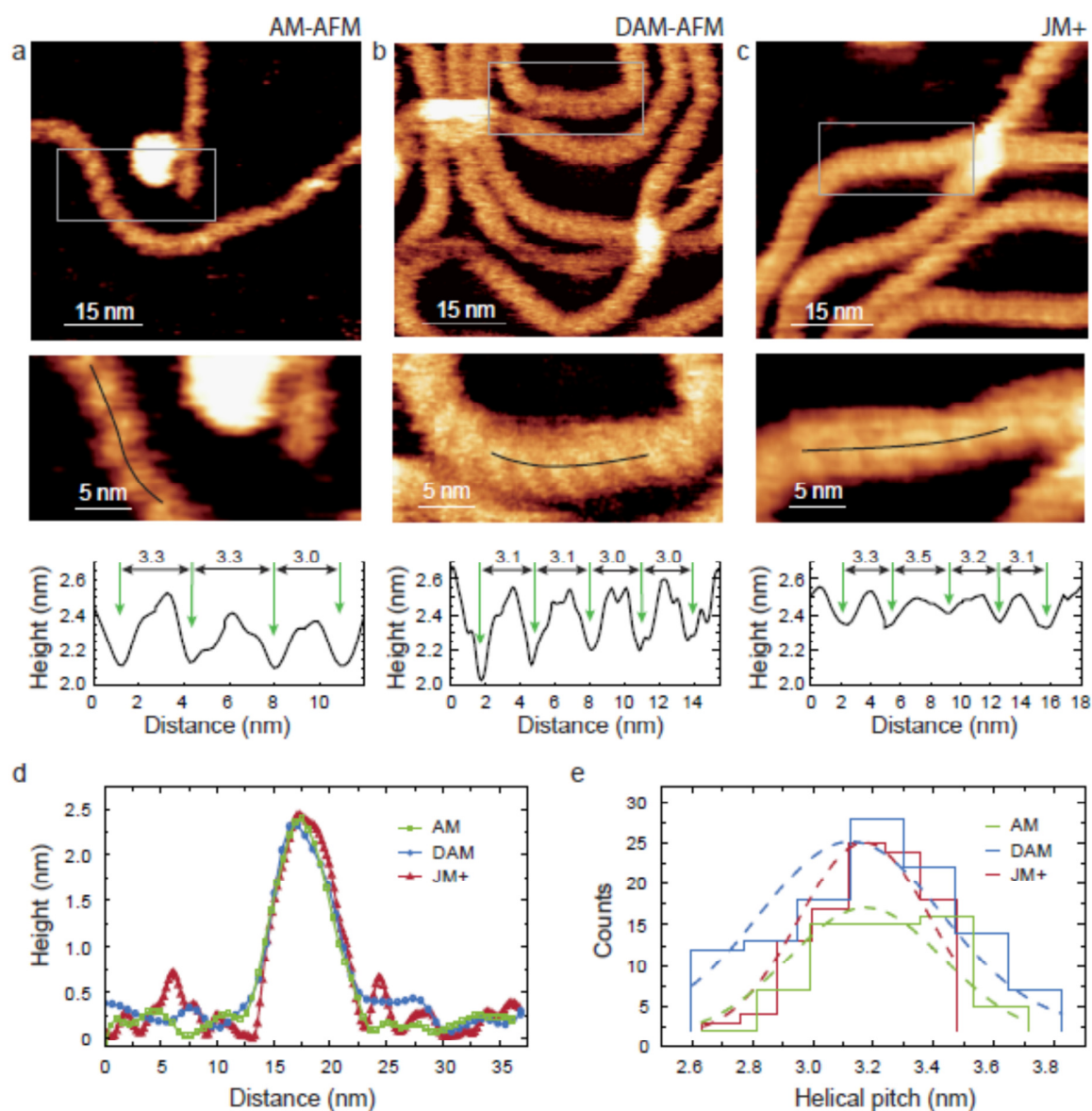


Fig. 3. High-resolution AFM images of dsRNA acquired in different imaging modes. (a) Amplitude Modulation, AM-AFM. (b) Drive Amplitude Modulation, DAM-AFM. (c) Jumping Mode plus, JM+. Top row: large field of view including several dsRNA molecules. Middle row: details at higher magnification of the squared region shown in the top row. Bottom row: height profiles along the lines depicted in the zoom-in images. Color scale was adjusted to enhance the corrugation observed along the dsRNA. (d) Cross-section profiles of dsRNA molecules imaged with AM-AFM, DAM-AFM, and JM+. (e) Histograms of the helical pitch for each of the three measuring modes employed in this work. Data was taken along different segments of the same molecule and on different molecules. Gaussian fits (dashed lines) provided mean \pm sd values of 3.2 ± 0.3 , 3.1 ± 0.4 , and 3.2 ± 0.3 nm, for AM-AFM, DAM, and JM+ imaging modes, respectively.

Our measurements were performed with commercial cantilevers specially chosen to image soft samples in liquid environments as they combine relatively high resonance frequencies and low spring constants. These tips allowed minimization of tip-sample interaction forces in both dynamic, using low oscillation amplitudes of $\lesssim 1$ nm, and in force-distance based modes, using set-point forces of tens of pN (see **Table 1** and **S1** for details). However, simulated AFM images (see Experimental section) clearly showed that it is not possible to obtain sub-helical pitch resolution with tips of nominal radius of 8 nm (**Fig. S1**). We therefore decided to further explore the role played by the dimensions of the tip in the achievement of the observed high resolution. AFM images of dsDNA and dsRNA structures were simulated using the atomic coordinated data provided by 3D-Dart software,³⁰ and dilated with tips of different radii. Similar simulation procedures have been also applied to dsDNA^{21, 24} and, despite being a qualitative model, it was enough to illustrate the importance of the tip apex size to image nucleic acid molecules. A model comprising realistic physical interactions between tip and sample is beyond the scope of this work. We then compared the full width at half-maximum of cross sectional profiles of the simulated images with the experimental data (**Fig. 4**). We found that the resolution achieved in the images where both major and minor grooves were visible was obtained with tips of radii 0.7-1.2 nm. Tips with larger radii (2.7-5.5 nm) led to images where only a single periodicity was detected (**Fig. 4**). Importantly, these simulation data indicated that the experimental images were obtained with a much sharper tip than specified by the manufacturer. A larger resolution than expected from a commercial tip has been reported before with other biological materials. Some examples include the observation of single monomers at the surface of viral particles,³¹ the visualization of single antibody subunits,³² or the detection of conformational changes in two-dimensional crystals of membrane proteins.³³ A likely explanation, already suggested by other authors, could be that the high resolution arises from a single protrusion or an impurity attached to the AFM tip.^{16, 24} In any case, our simulation data highlights the relevance of the tip apex size to image nucleic acids.

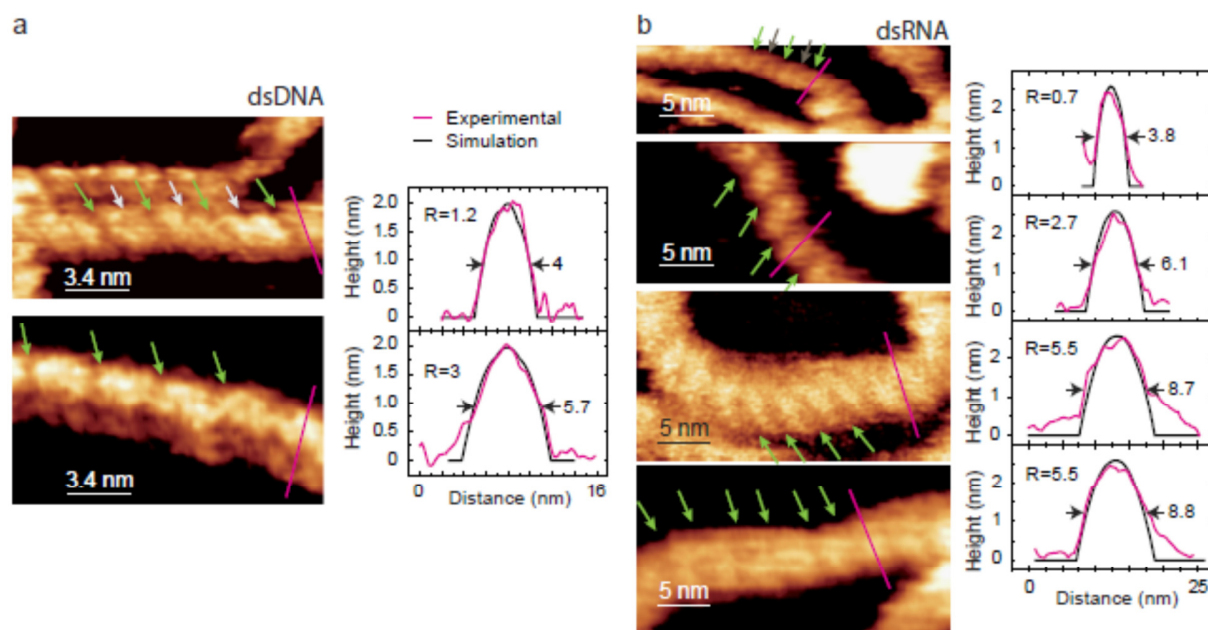


Fig. 4. *dsDNA and dsRNA high-resolution imaging dependence with the tip radius.* (a) Data relative to dsDNA. Simulated AFM images with a tip radius of 1.2 nm provided a similar experimental cross-sectional profile in images where both major and minor grooves were visible. Images where only the major groove was resolved provided an estimation for the tip radius of 3.0 nm. (b) Data relative to dsRNA. Images where both the major and minor grooves were visible provided an estimation for the tip radius of 0.7 nm. Images where single periodicity was observed provided an estimation for the tip radius of 2.7 and 5.5 nm. Lines across the molecules correspond to the experimental profiles. Full width at half maximum is also shown in nanometers.

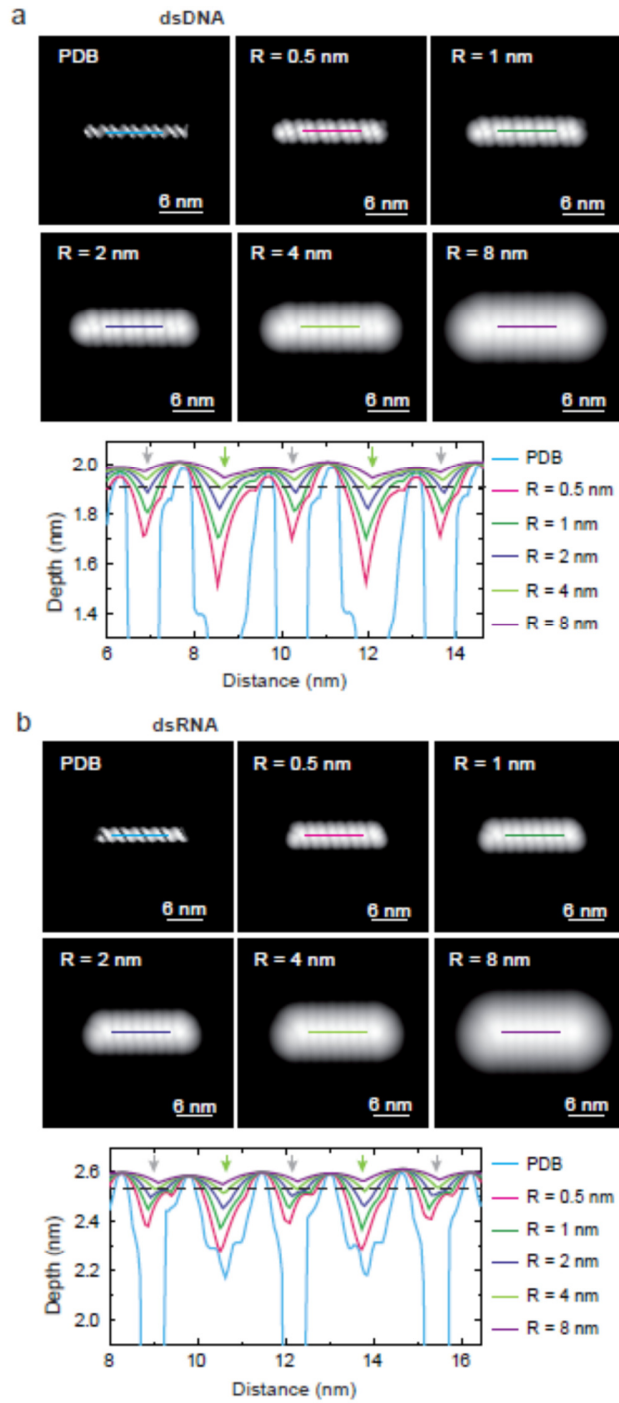


Fig. 5. Simulations of AFM images of dsDNA and dsRNA. **(a)** dsDNA. **(b)** dsRNA. Top row: simulated AFM topographic images for different tip radius. Bottom row: height profiles taken in the central part of the molecule along the longitudinal axis of the simulated images. The height interval has been adjusted equally for dsDNA and dsRNA to improve visualization of the penetration depths of profiles for the different tip radii. Dashed line represents the minimum depth experimentally observable according to the Rose criterion (see main text).

In order to determine which of the two grooves are observed in the images, we calculated the longitudinal profile in simulated AFM images for different tip radius and compared the depth of the tip penetration in the groove with the vertical noise of our instrument. The vertical noise was estimated from a recording of the Z-dimension on a flat clean surface for two minutes under high-resolution imaging conditions (**Supplementary methods**). The height distribution was fitted by a Gaussian function giving a RMS noise value of 0.3 Å (**Fig. S2**). According to the Rose criterion, for a signal to be distinguished from the noise, the ratio between the power of the signal and the noise (SNR) should be larger than 5.^{34, 35} Considering that amplitudes follow a square root relationship with power, we conclude that the minimum depth to be resolved with our experimental height is ~0.7 Å. The implication is that only corrugations deeper than 0.7 Å will be visible. AFM images of dsDNA and dsRNA structures were simulated using the atomic coordinated data provided by 3D-Dart software,³⁰ and convoluted with tips of different radii (**Fig. 5**). The 0.7 Å threshold rule (dashed line in **Fig. 5**) led to the conclusion that both major and minor grooves can only be visible when the tip radius is $\lesssim 2.5$ nm, in agreement with our previous observation comparing experimental and simulated data. As expected, the simulation data of dsDNA and dsRNA showed a decrease of the apparent depth of both major and minor grooves with increasing tip radius. In dsDNA simulations the major groove always looked deeper than the minor groove independently of the tip radius used. Therefore, as the tip radius increases, the ability to resolve the minor groove gradually reduces. However, in the case of dsRNA, this observation is not that obvious because as the tip radius increases both grooves present the same apparent depth (see for instance profiles for $R = 4$ nm and $R = 8$ nm). So, we cannot give a clear answer regarding which of the two grooves is observed in the dsRNA images that show the single 3.1 nm periodicity (**Fig. 3**). Still, for very sharp tips the major groove is slightly favored with respect to the minor as it occurs with dsDNA.

CONCLUSIONS

We report here the first sub-helical resolution images of individual double-stranded RNA molecules obtained with AFM. We have resolved both minor and major grooves and we have quantified the helical pitch using different dynamic and force-based imaging modes, resulting in 3.1 ± 0.3 nm, compatible with the A-form of dsRNA. Data obtained with the three imaging modes employed here have shown similar resolution at optimized working conditions. Simulated AFM images have allowed us to estimate the tip radius employed for high-resolution imaging, showing that radii as small as 2.5 nm are needed to discriminate both major and minor grooves. Use of slightly larger radii leads to the observation of a single periodicity in both samples. According to the simulations, this single periodicity corresponds to the major groove in the case of dsDNA but it is not clear which groove is observed in the case of dsRNA. Finally, we conclude that two aspects are critical to obtain high resolution of nucleic acids in liquid. Firstly, the interacting force, that can be minimized with the proper tuning of each imaging mode parameters, and secondly, the sharpness of the tip, which likely arises from a protrusion or a small feature located at the apex of tip of the relatively blunt commercial cantilevers.

Experimental.

dsDNA and dsRNA molecules.

As dsDNA sample we used the plasmid pGEM3Z (2743 bp, promega) linearized with *Bam*HI and purified with a QIAquick PCR purification kit (Qiagen, Hilden, Germany). dsRNA molecules were fabricated as described in ².

dsDNA and dsRNA sample preparation.

Freshly-cleaved mica sheets were first treated with 10 μ l of Buffer A (10 mM NiCl_2 and 10 mM Tris-HCl pH 8.0). Then, 1 μ l (0.6 ng) of dsRNA or dsDNA was added to the droplet and incubated for 15 minutes at room temperature. After incubation, 40 μ l of Buffer A was added to the sample and then completed with 50 μ l of Buffer B (10 mM TrisHCl pH 8.0) to reach a final volume of 100 μ l.

AFM imaging.

A Cervantes FullMode AFM from Nanotec Electronica equipped with a cantilever holder specially designed for dynamic mode imaging in liquids was used.³⁶ High resolution images were obtained in a setup with the microscope placed into an acoustic isolation enclosure with a passive anti-vibration system. It incorporates a homemade temperature control system to image at a constant temperature of 16°C below room temperature to minimize thermal drift and to reduce liquid evaporation. This contributed to improve the quality of our images and to scan the sample for long periods of time. WSxM software (www.wsxmsolutions.com) was employed to both the acquisition and the post-processing of the AFM images.³⁷ Commercial Biolever mini BL-AC40TS-C2 cantilevers from Olympus (<http://probe.olympus-global.com/en/>) were used for all the measurements. Nominal parameters of these cantilevers: resonance frequency in air 110 kHz, resonance frequency in liquid 25 kHz, spring constant $0.09 \text{ N}\cdot\text{m}^{-1}$ and tip radius 8 nm. Each of the cantilevers spring constant was calibrated following Sader's method³⁸ yielding spring constants of $0.07 \pm 0.01 \text{ N}\cdot\text{m}^{-1}$. The deflection sensitivity of the optical detection system was calibrated from force curves, resulting in $\sim 9 \text{ nm/V}$. This very low value proved to be crucial to control the low amplitudes and forces required for high resolution imaging. The piezo scanner was calibrated with two AFM gratings with pitch distances 3 μm (TGX01, Mikromasch) and 300 nm (2D300, Nanosensors) and, Highly Oriented Pirolytic Graphite (HOPG, SPI supplies), with an atomic periodicity of 0.25 nm. The three different calibration constants obtained for the X-Y directions of the piezo were found to linearly depend with the scanning size. The parameters of the linear fit were introduced in the control software of the AFM, which automatically adapts the piezo driving voltages to the required scanning size.

AM-AFM and DAM-AFM experiments (see **Fig. S3** for a cartoon with the operational configuration of these imaging modes) were carried out using piezo-acoustic excitation. We employed a cantilever holder that minimizes the spurious resonance frequencies that often appear when working in liquids (see ESI of ref. 39). This allowed us to determine the resonance frequency from a frequency sweep in good agreement with the resonance frequency value obtained by measuring the cantilever thermal noise. The cantilever free amplitude for the approach was set to a relatively high value of $\sim 7 \text{ nm}$, with a set point

of about 75% of the free amplitude. With these settings, using the *Full Auto Approach* option in the WSxM software no false engagements were detected. Once engaged, the drive amplitude was changed to reduce the cantilever amplitude to imaging values (0.6-0.7 nm) and the set-point was also reduced accordingly, to remain just below the amplitude value at which the cantilever was lifted off the sample. For AM-AFM imaging, scanning was initiated immediately after the approach, adjusting the set-point and the feedback gains to values that optimize image acquisition with no sample damage, judged from repetitive imaging of the same area.

DAM-AFM imaging required the setting of its proper feedback scheme after tip engagement.²² This step was done with the tip withdrawn 900 nm from the sample. A Phase Lock Loop (PLL) was used to track the resonance frequency and two nested feedback loops give the topography. The first loop adjusts the drive amplitude in order to maintain the cantilever oscillation amplitude. The drive amplitude needed to sustain this oscillation amplitude is related to the energy dissipated in the tip-sample interaction. By regulating the position of the scanner in the z-direction the drive amplitude is kept constant at the set-point value. Thus, the energy of the cantilever is automatically adapted at each point. As before, set-points and feedback gains of the different loops were adjusted to optimize the imaging acquisition with no sample damage. Very low dissipation set-points were used (~0.3 fW), but they proved sufficient to automatically adapt the cantilever energy at each point of the image without being trapped by the attractive forces.

JM+ experiments were carried out by performing a quick force vs. distance curve (FZ) at each point of the scanned area, moving the tip laterally at the farthest tip-sample distance minimizing lateral forces. The tip-sample feedback is set by the peak force as referenced to the force baseline. JM+ removes the dragging force, detecting accurately the tip-sample contact, thus minimizing the scanning forces.²⁶ The tip-sample coarse approach was performed in AM-AFM mode and, once in range, the cantilever oscillation was removed. Following this procedure, forces during coarse approach are minimized. JM+ set points in the range of 0.05-0.07 V, corresponding to forces of the order of 35-50 pN, and Z excursions in the range of 15-35 nm were used for imaging. See **Fig. S3** for a cartoon depicting the operational configuration of this imaging mode.

Regardless of the imaging mode employed, once the tip was in range, we first scanned an area of $1 \times 1 \mu\text{m}^2$ at low resolution to locate molecules with straight segments over several tens of nm. Higher resolution images were recorded at scan sizes of $50 \times 50 - 150 \times 150 \text{ nm}^2$, 512×512 pixels (pixel resolution between 0.1 and $0.3 \text{ nm}\cdot\text{pix}^{-1}$) and scanning frequencies of $3-8 \text{ lines}\cdot\text{s}^{-1}$. The fast scan direction was preferably set to be parallel to these segments to minimize low frequency noise and to facilitate the helical pitch visualization. Indeed, helical pitch visualization was easier along the fast scan axis but it was also possible to observe the periodicity of dsRNA and dsDNA along molecules not aligned to the horizontal direction of the image (**Fig. 1a** and **Fig. 3a**). To check for consistency of the observed topographic features, initially each scan line in the image was scanned from left to right (trace direction) and from right to left (retrace direction). Then, in order to increase the scan rate, images were only acquired in trace direction.

Image analysis.

Raw images were subjected to the following standard procedures implemented in WSxM software: flatten plus background subtraction, artifact lines removal produced by tip attachments, and Gaussian filtering. WSxM software was also employed to obtain the cross-sectional and longitudinal profiles along the molecules and to measure distances along these profiles.

The color scale of the images shown in the manuscript were adjusted to enhance the corrugation of the upper region of the molecules. Therefore, all data below a certain threshold appear black. The residual roughness of the substrate can be appreciated in **Fig. S4** that shows images of **Fig. 3** with a full height color scale. We have measured the RMS roughness on clean areas (no DNA or RNA) and obtained a value of 0.33 ± 0.06 nm, an order of magnitude lower than the molecule diameter.

In order to discard any influence of a hypothetical substrate roughness periodicity on the observed dsDNA/dsRNA corrugation, we performed Fourier analysis of molecule-free images (**Fig. S5**). We computed the angle-integrated power spectral density (PSD) of the image. The angle-integrated PSD on these clean regions did not show the predominance of any particular wavelength. Moreover at the periodicity of interest of our study, *i.e.*, 3.4 nm and 3.1 nm for dsDNA and dsRNA, the amplitude of the corrugation was negligible (See ESI Methods for more details).

3D models of dsDNA and dsRNA.

We used a fragment of 48-mer poly A-T sequence for both structures but represented as B-form, for dsDNA, or A-form, for dsRNA. The molecular structure in PDB format was produced using 3D-Dart software.³⁰

AFM images simulation and tip dilation.

Graphical representations of the dsDNA and dsRNA crystal structures were generated using the UCSF Chimera package.⁴⁰ These graphics were represented in a grayscale chosen to represent the height of the structures. Top views were selected and then TIFF files generated. These TIFF files were imported in WSxM, obtaining in this way AFM-like images of the crystal structures. Images were dilated using the tip-sample dilation option in WSxM. The dilation algorithm uses a parabolic tip of radius r , with $z = \frac{x^2+y^2}{2r}$, where xyz are the lateral and vertical coordinates of the image.⁴¹ Dilation simulations treated both tip and molecule as hard undeformable bodies.

Author Contributions

F. M.-H., J. G.-H., and P.A wrote the paper that was further revised and accepted by all authors. F. M.-H., J. G.-H., A. G., M.E. F.-P and P.A. proposed the experimental work. P.A. and M.E. F.-P. did the AFM experiments and analyzed the data. P.A. did the AFM simulations. E. H.-G. and J.M.V. prepared the dsRNA sample.

Acknowledgements

We thank Pedro J. de Pablo for support and discussions. We acknowledge Alejandro Martín and Cesar L. Pastrana for experimental assistance in some experiments and for the preparation of the 3D models of dsDNA and dsRNA.

This work was supported by the European Research Council (grant 206117 SM-DNA-REPAIR to F.M.-H.), the Spanish Ministry of Economy and Competitiveness (grants FIS2014-58328-P and FIS2014-51481-ERC to F.M.-H., grant Consolider CSD2010-0024 to J.G.-H. and grant BFU2013-44202 to J.M.V.) and the Madrid Regional Government (grant MAT2013-46753-C2-2 to J.G.-H. and S2013/MIT-2807 to J.M.V.).

Notes and References

1. J. A. Abels, F. Moreno-Herrero, T. van der Heijden, C. Dekker and N. H. Dekker, *Biophys J*, 2005, **88**, 2737-2744.
2. E. Herrero-Galan, M. E. Fuentes-Perez, C. Carrasco, J. M. Valpuesta, J. L. Carrascosa, F. Moreno-Herrero and J. R. Arias-Gonzalez, *J Am Chem Soc*, 2013, **135**, 122-131.
3. J. Lipfert, G. M. Skinner, J. M. Keegstra, T. Hensgens, T. Jager, D. Dulin, M. Kober, Z. Yu, S. P. Donkers, F. C. Chou, R. Das and N. H. Dekker, *Proc Natl Acad Sci U S A*, 2014, **111**, 15408-15413.
4. J. Mou, D. M. Czajkowsky, Y. Zhang and Z. Shao, *FEBS Lett*, 1995, **371**, 279-282.
5. F. Moreno-Herrero, J. Colchero, J. Gomez-Herrero and A. M. Baro, *Phys Rev E Stat Nonlin Soft Matter Phys*, 2004, **69**, 031915.
6. Y. L. Lyubchenko and L. S. Shlyakhtenko, *Methods*, 2009, **47**, 206-213.
7. V. Cassina, M. Manghi, D. Salerno, A. Tempestini, V. Iadarola, L. Nardo, S. Brioschi and F. Mantegazza, *Biochim Biophys Acta*, 2015, DOI: 10.1016/j.bbagen.2015.10.006.
8. Q. Zhong, D. Inniss, K. Kjoller and V. B. Elings, *Surface Science*, 1993, **290**, L688-692.
9. P. K. Hansma, J. P. Cleveland, M. Radmacher, D. A. Walters, P. E. Hillner, M. Bezanilla, M. Fritz, D. Vie, H. G. Hansma, C. B. Prater, J. Massie, L. Fukunaga, J. Gurley and V. Elings, *Appl. Phys. Lett.*, 1994, **64**, 1738-1740.
10. D. J. Müller, D. Fontiadis, S. Scheuring, S. A. Müller and A. Engel, *Biophys. J.*, 1999, **76**, 1101-1111.
11. H. Yamashita, K. Voitchovsky, T. Uchihashi, S. A. Contera, J. F. Ryan and T. Ando, *J Struct Biol*, 2009, **167**, 153-158.
12. I. Casuso, J. Khao, M. Chami, P. Paul-Gilloteaux, M. Husain, J. P. Duneau, H. Stahlberg, J. N. Sturgis and S. Scheuring, *Nat Nanotechnol*, 2012, **7**, 525-529.
13. N. Kodera, D. Yamamoto, R. Ishikawa and T. Ando, *Nature*, 2010, **468**, 72-76.
14. M. Maaloum, A. F. Beker and P. Muller, *Phys Rev E Stat Nonlin Soft Matter Phys*, 2011, **83**, 031903.
15. M. Kitazawa, S. Ito, A. Yagi, N. Sakay, Y. Uekusa, R. Ohta, K. Inaba, A. Hayashi, Y. Hayashi and M. Tanemura, *Japanese Journal of Applied Physics*, 2011, **50**, S3.
16. C. Leung, A. Bestembayeva, R. Thorogate, J. Stinson, A. Pyne, C. Marcovich, J. Yang, U. Drechsler, M. Despont, T. Jankowski, M. Tschope and B. W. Hoogenboom, *Nano Lett*, 2012, **12**, 3846-3850.
17. A. Pyne, R. Thompson, C. Leung, D. Roy and B. W. Hoogenboom, *Small*, 2014, **10**, 3257-3261.
18. O. Marti, B. Drake and P. K. Hansma, *Appl. Phys. Lett.*, 1987, **51**, 484-486.

19. D. Martinez-Martin, C. Carrasco, M. Hernando-Perez, P. J. de Pablo, J. Gomez-Herrero, R. Perez, M. G. Mateu, J. L. Carrascosa, D. Kiracofe, J. Melcher and A. Raman, *PLoS One*, 2012, **7**, e30204.
20. T. Fukuma and S. P. Jarvis, *Review of Scientific Instruments*, 2006, **77**, 043701.
21. H. Yamada, K. Kobayashi, T. Fukuma, Y. Hirata, K. T. and K. Matsushige, *Applied Physics Express*, 2009, **2**, 095007.
22. M. Jaafar, D. Martinez-Martin, M. Cuenca, J. Melcher, A. Raman and J. Gomez-Herrero, *Beilstein journal of nanotechnology*, 2012, **3**, 336-344.
23. F. J. Giessibl, H. Bielefeldt, S. Hembacher and J. Mannhart, *Applied Surface Science*, 1999, **140**, 352-357.
24. S. Ido, K. Kimura, N. Oyabu, K. Kobayashi, M. Tsukada, K. Matsushige and H. Yamada, *ACS Nano*, 2013, **7**, 1817-1822.
25. Y. F. Dufrene, D. Martinez-Martin, I. Medalsy, D. Alsteens and D. J. Muller, *Nat Methods*, 2013, **10**, 847-854.
26. A. Ortega-Esteban, I. Horcas, M. Hernando-Perez, P. Ares, A. J. Perez-Berna, C. San Martin, J. L. Carrascosa, P. J. de Pablo and J. Gomez-Herrero, *Ultramicroscopy*, 2012, **114**, 56-61.
27. J. Melcher, D. Martinez-Martin, M. Jaafar, J. Gomez-Herrero and A. Raman, *Beilstein journal of nanotechnology*, 2013, **4**, 153-163.
28. M. Maaloum, *Eur Biophys J*, 2003, **32**, 585-587.
29. F. Moreno-Herrero, J. Colchero and A. M. Baro, *Ultramicroscopy*, 2003, **96**, 167-174.
30. M. van Dijk and A. M. Bonvin, *Nucleic Acids Res*, 2009, **37**, W235-239.
31. M. Hernando-Perez, E. Pascual, M. Aznar, A. Ionel, J. R. Caston, A. Luque, J. L. Carrascosa, D. Reguera and P. J. de Pablo, *Nanoscale*, 2014, **6**, 2702-2709.
32. A. San Paulo and R. Garcia, *Biophys. J.*, 2000, **78**, 1599-1605.
33. D. J. Muller, A. Engel, J. L. Carrascosa and M. Velez, *Embo J*, 1997, **16**, 2547-2553.
34. A. Rose, *Vision: Human and Electronic (Optical Physics and Engineering)*, Springer, 1973.
35. J. T. Bushberg, *The Essential Physics of Medical Imaging*, Lippincott Williams & Wilkins, 2002.
36. C. Carrasco, P. Ares, P. J. de Pablo and J. Gomez-Herrero, *Rev Sci Instrum*, 2008, **79**, 126106.
37. I. Horcas, R. Fernandez, J. M. Gomez-Rodriguez, J. Colchero, J. Gomez-Herrero and A. M. Baro, *Rev Sci Instrum*, 2007, **78**, 013705.
38. J. E. Sader, *Journal of Applied Physics*, 1998, **84**, 64.
39. P. Ares, M. Jaafar, A. Gil, J. Gomez-Herrero and A. Asenjo, *Small*, 2015, **11**, 4731-4736.
40. E. F. Pettersen, T. D. Goddard, C. C. Huang, G. S. Couch, D. M. Greenblatt, E. C. Meng and T. E. Ferrin, *Journal of computational chemistry*, 2004, **25**, 1605-1612.
41. J. S. Villarrubia, *J. Vac. Sci. Technol. B*, 1996, **14**, 1518-1521.